Nanosecond optical parametric oscillator with 90° image rotation: design and performance

Arlee V. Smith and Darrell J. Armstrong

Department 1118, Sandia National Laboratories, Albuquerque, New Mexico 87185-1423

Received January 22, 2002; revised manuscript received April 29, 2002

According to numerical models of nanosecond optical parametric oscillators, cavities with 90° image rotation can produce high-quality beams even if the Fresnel number of the cavity is large. We review the properties of such image-rotating cavities and present a method for designing them. The laboratory performance of one promising design is characterized, demonstrating its ability to produce high-quality beams with good efficiency.

OCIS codes: 140.3410, 140.4780, 190.4970.

1. INTRODUCTION

The design of nanosecond optical parametric oscillators (OPOs) is constrained by optical damage limits of 1–10 J/cm^2 for 5–20-ns pulses and by the requirement of short cavity length for high efficiency. These constraints imply that scaling a nanosecond OPO to high pulse energy entails increasing the beam diameters to avoid damage while keeping the cavity short. The result is a high-Fresnel-number cavity ($N_F = d^2/\lambda L$, where d is the beam diameter and L is the cavity length) with subsequent poor diffractive coupling across the transverse profiles. This is a recipe for poor beam quality. Confocal unstable resonators have proven their worth in improving the beam quality of high-Fresnel-number nanosecond lasers. Recently they have been applied to nanosecond OPOs as well. Hansson *et al.*[1] used an unstable resonator with a Fresnel number of ~250 and magnification of 1.2 around a periodically poled $RbTiOAsO_4$ crystal to achieve a factor of 3 improvement in M^2 over a comparable resonator without magnification. This replicates similar results with noncritically phase-matched $KTiOPO_4$ by Farmer *et al.*[2] Unstable resonators are best suited to quasi-phase-matched or noncritically phase-matched crystals because the pump can be double passed without problems of acceptance angle on the diverging backward-propagating beams. Such double passing of the pump makes possible high conversion efficiency. However, Johnson *et al.*[3] used an unstable resonator with critically phase-matched β-BaB_2O_4 and single-pass pumping to produce a better-quality beam than without magnification.

Apart from the unstable-resonator designs, there have been few careful studies devoted to beam-quality improvement in high N_F OPOs. In an earlier paper[4] we systematically examined several alternative OPO designs that promise improved beam quality for critically phase-matched crystals. Among these designs is the one implemented by Anstett *et al.*[5] Their large N_F OPO used a retroreflecting prism as a backmirror and double passed the pump to demonstrate dramatic beam-quality improvement over comparable OPOs without these two features. Their operating parameters and measured beam quality ($M^2 \approx 3.5$) were comparable to those achieved with the new design that we will describe in this paper. Our new design uses a four-mirror ring to produce true 90° image rotation. It has several attractive features. Most importantly, according to our modeling studies, it can produce highly symmetric signal beams with good beam quality even for large N_F. In an earlier study[6] we characterized the performance of a related design, a three-mirror ring OPO that used an intracavity Dove prism to achieve image rotation. That design is equivalent to a six-mirror nonplanar ring. It produced the predicted high-quality signal beams, improving on comparable non-image-rotating designs, but, because it had a relatively long cavity, its conversion efficiency was relatively low. The new four-mirror ring permits shorter cavities. In this paper we investigate the general properties of image-rotating nonplanar cavities and explain how to design them. We choose one promising four-mirror design and compare its laboratory performance with the predictions of our OPO model, demonstrating excellent beam quality and high efficiency for large Fresnel numbers.

2. IMAGE-ROTATING CAVITY DESIGN

A. Calculation of Image-Rotation Angle

We will review one method for calculating the image-rotation angle of a nonplanar ring cavity[7] composed of flat mirrors. First, we develop a mathematical formalism for mirror reflections, then we apply it to a nonplanar ring, and then we show how the rotation angle can be calculated from the area bounded by great arcs connecting propagation directions on the unit sphere. We consider only the transformation of images, ignoring for now the phases of the optical fields and thus their polarizations. These will be discussed later.

Figure 1(a) shows an example of image rotation due to a pair of nonplanar reflections. An image is shown incident upon mirror M_1 along with a coordinate system $[X, Y]$ oriented so its Y axis lies in the plane of incidence

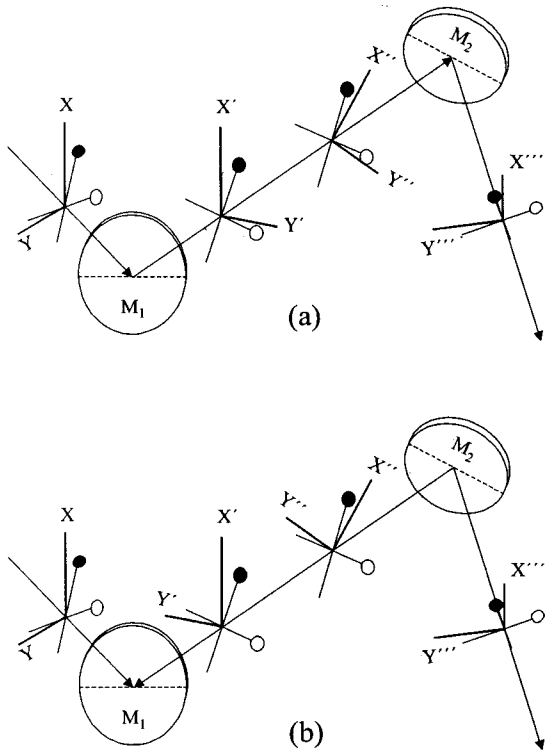

Fig. 1. (a) Diagram of reference frame and image rotation for successive reflections with nonparallel planes of incidence, and (b) the same diagram showing the reversed propagation vector for the second leg. The sense of rotation as measured in the lower diagram is opposite that measured in the upper diagram. A counterclockwise rotation of the reference frame in the lower diagram corresponds to a clockwise image rotation in going from the initial to the final reference plane.

of M_1 and its Z axis lies along the propagation direction. The plane of incidence is the plane containing the propagation vector of the incident beam and the normal to the mirror face. After reflection from mirror M_1, the right-handed reference frame with Z' aligned along the new propagation direction and Y' in the plane of incidence is the one labeled $[X', Y']$. In this coordinate system the y values of the image are reversed relative to those of the original coordinate system $[X, Y]$, but the x values are not. An image point with coordinates (x, y) in frame $[X, Y]$ is transformed to $(x, -y)$ in frame $[X', Y']$. This mirror transformation can be written

$$\begin{bmatrix} x' \\ y' \end{bmatrix} = \begin{bmatrix} x \\ -y \end{bmatrix} = M \begin{bmatrix} x \\ y \end{bmatrix} \tag{1}$$

so the mirror transformation matrix is

$$M = \begin{bmatrix} 1 & 0 \\ 0 & -1 \end{bmatrix}. \tag{2}$$

The reflection at mirror M_2 is handled by first changing to the double-primed reference frame oriented so the Y'' axis lies in the plane of incidence of M_2, followed by mirror reflection to place the image in the triple-primed reference frame. The transformation to the double-primed frame requires rotation about the propagation direction by angle γ, the angle between the planes of incidence for mirrors M_1 and M_2. This transformation is described by

$$\begin{bmatrix} x'' \\ y'' \end{bmatrix} = R \begin{bmatrix} x' \\ y' \end{bmatrix}, \tag{3}$$

where the rotation matrix R is

$$R = \begin{bmatrix} \cos\gamma & \sin\gamma \\ -\sin\gamma & \cos\gamma \end{bmatrix}. \tag{4}$$

Just as at mirror M_1 the reflection is described by

$$\begin{bmatrix} x''' \\ y''' \end{bmatrix} = M \begin{bmatrix} x'' \\ y'' \end{bmatrix}, \tag{5}$$

so the total transformation from the initial to final reference frame is

$$\begin{bmatrix} x''' \\ y''' \end{bmatrix} = MRM \begin{bmatrix} x \\ y \end{bmatrix}. \tag{6}$$

These transformations can be applied to a set of mirrors that form a resonant cavity, in which case the initial and the final reference frames may be chosen to be identical. For example, with a four-mirror cavity the transformation is

$$\begin{bmatrix} x_1 \\ y_1 \end{bmatrix} = MR_{41}MR_{34}MR_{23}MR_{12} \begin{bmatrix} x_0 \\ y_0 \end{bmatrix}, \tag{7}$$

where (x_0, y_0) is the coordinate of a point in the initial frame and (x_1, y_1) is its coordinate after a trip around the cavity. We can rewrite this as

$$\begin{bmatrix} x_1 \\ y_1 \end{bmatrix} = (MR_{41}M)R_{34}(MR_{23}M)R_{12} \begin{bmatrix} x_0 \\ y_0 \end{bmatrix}. \tag{8}$$

Applying the relation

$$\begin{aligned} (MRM) &= \begin{bmatrix} 1 & 0 \\ 0 & -1 \end{bmatrix} \begin{bmatrix} \cos\gamma & \sin\gamma \\ -\sin\gamma & \cos\gamma \end{bmatrix} \begin{bmatrix} 1 & 0 \\ 0 & -1 \end{bmatrix} \\ &= \begin{bmatrix} \cos\gamma & -\sin\gamma \\ \sin\gamma & \cos\gamma \end{bmatrix} = R^{-1}, \end{aligned} \tag{9}$$

this becomes

$$\begin{bmatrix} x_1 \\ y_1 \end{bmatrix} = R_{41}^{-1}R_{34}R_{23}^{-1}R_{12} \begin{bmatrix} x_0 \\ y_0 \end{bmatrix}. \tag{10}$$

Thus odd-numbered mirrors are associated with a rotation R_{ij}, whereas the even-numbered mirrors are associated with an inverse rotation R_{ij}^{-1}. However, if we change our reference frame for the even legs so $\hat{z}$ is directed opposite the propagation direction, as shown in Fig. 1(b), the sense of rotation is reversed, and we can write this as

$$\begin{bmatrix} x_1 \\ y_1 \end{bmatrix} = \bar{R}_{41}R_{34}\bar{R}_{23}R_{12} \begin{bmatrix} x_0 \\ y_0 \end{bmatrix}, \tag{11}$$

where $\bar{R}_{ij}$ indicates a rotation angle measured about the reversed propagation vector for the even legs. Note that if the cavity has an even number of mirrors, the groupings of transformation matrices illustrated in Eq. (8) makes it clear that the image undergoes a true rotation. However, if the cavity consists of an odd number of mirrors, there is an extra M, and the image undergoes rotation plus a mirror inversion. Such pseudorotations are not expected to be effective in beam cleanup unless walk-off-compensating crystals are used. In the remainder of

this paper we will consider only four-mirror rings, so the image rotations are true rotations.

Clearly the round-trip image-rotation angle for a cavity is the sum of the angles between the planes of incidence for consecutive cavity mirrors, with the angle convention just described, where even- and odd-numbered legs use opposite $\hat{z}$ directions. For convenience in performing this sum, the plane of incidence for each mirror can be conveniently shown on the unit sphere. As an example, we consider the nonplanar ring shown in Fig. 2, where light circulates from mirror M_1 to M_2 to M_3 to M_4. In Fig. 3(a) we plot the four unit vectors $\hat{k}_1$, $-\hat{k}_2$, $\hat{k}_3$, $-\hat{k}_4$ in a transparent unit sphere. The plane of incidence for M_1 is the plane containing $-\hat{k}_4$ and $\hat{k}_1$. The angle of incidence on M_1 is half the great arc connecting the end points of $-\hat{k}_4$ and $\hat{k}_1$. Similarly, the plane of incidence for M_2 is the plane containing $\hat{k}_1$ and $-\hat{k}_2$. The image-rotation angle is the negative of the angle between the planes of incidence for mirrors M_1 and M_2, indicated in the diagram by γ_1. The round-trip rotation angle is given by

$$\Theta = -(\gamma_1 + \gamma_2 + \gamma_3 + \gamma_4). \tag{12}$$

Redrawing the unit sphere as an opaque sphere in Fig. 3(b), we place point O somewhere inside the spherical quadrilateral formed by the ends of the k vectors, so we can rewrite the image-rotation angle Θ as

$$\Theta = A + B + C + D + E + F + G + H - 4\pi \tag{13}$$

$$= (A + B + I) + (C + D + J) + (E + F + K) + (G + H + L) - 6\pi. \tag{14}$$

According to Girard's formula, the area of a triangle on the unit sphere is the sum of its internal angles minus π, so the image-rotation angle, Θ, can be written in terms of the areas of spherical triangles as

$$\Theta = (\text{Area}_{\Delta QRO} + \text{Area}_{\Delta RSO} + \text{Area}_{\Delta STO} + \text{Area}_{\Delta TQO}) - 2\pi = \text{Area}_{\text{Quadrilateral}} - 2\pi, \tag{15}$$

and the image-rotation angle, modulo 2π, is simply the area of the quadrilateral traced on the unit sphere by the great arcs connecting propagation unit vectors $\hat{k}_1$, $-\hat{k}_2$, $\hat{k}_3$, $-\hat{k}_4$. The direction of rotation, that is, the sign of Θ, depends on whether the quadrilateral is traced clockwise or counterclockwise. Viewed from the origin of the sphere, a clockwise quadrilateral gives a clockwise image rotation as viewed along the propagation vectors $\hat{k}_1$ or $-\hat{k}_2$ or a counterclockwise rotation as viewed along $-\hat{k}_1$ or $\hat{k}_2$. The image rotation reflects the fact that the cav-

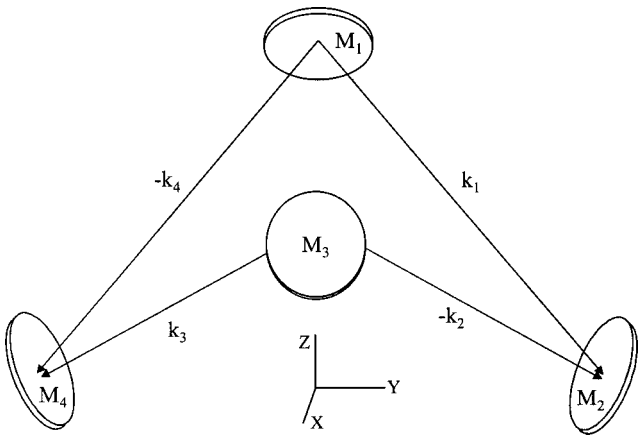

Fig. 2. Example of a four-mirror nonplanar ring resonator. The even-numbered propagation vectors are drawn reversed, as discussed in the text.

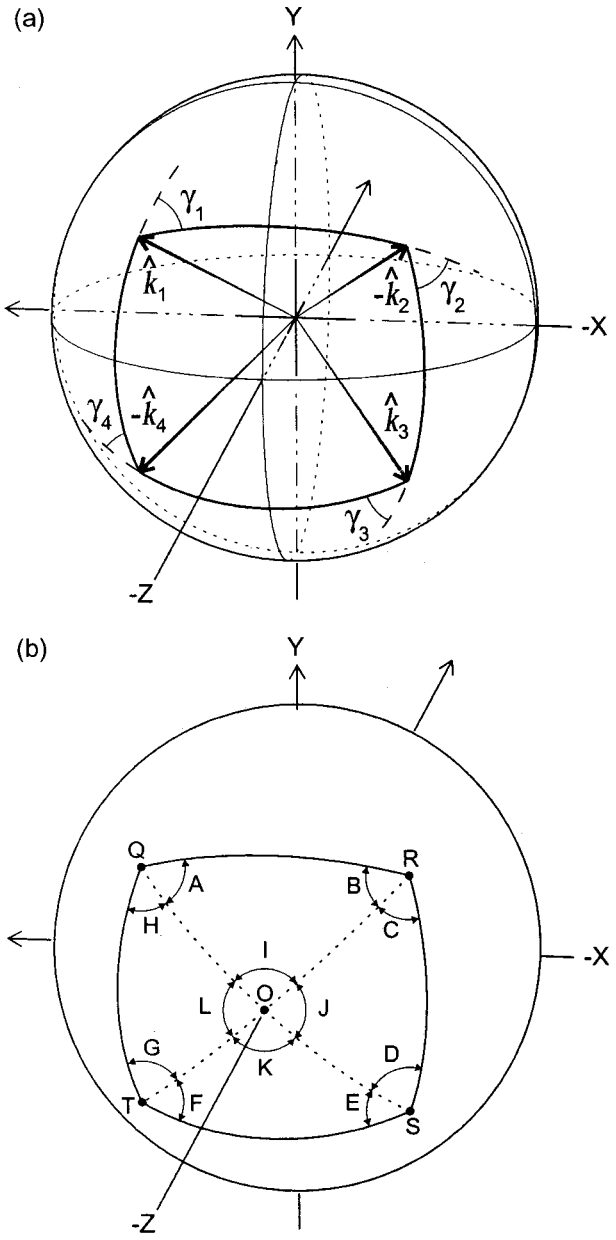

Fig. 3. Unit-sphere diagrams of the propagation vectors ($\hat{k}_1$, $-\hat{k}_2$, $\hat{k}_3$, $-\hat{k}_4$) for the cavity shown in Fig. 2. The upper figure (a) is drawn on a transparent sphere and shows great arcs connecting the tips of pairs of k vectors. These arcs lie in the plane of incidence for the corresponding reflection and have an are length equal to the reflection angle. The image-rotation angle for one pass of the resonator is given by $-(\gamma_1 + \gamma_2 + \gamma_3 + \gamma_4)$. The lower figure (b) is drawn on an opaque sphere and shows auxiliary arcs connecting the tip of each $\hat{k}$ vector with an auxiliary point O along with the labeling convention used in the text.

ity has a handedness or helicity. Its mirror image has the opposite handedness and rotates the image in the opposite direction.

The lengths of the cavity legs are constrained by the requirement that the cavity close on itself. For a four-mirror cavity with polar angles θ_i and ϕ_i for the unit vectors $\hat{k}_i$, this may be expressed in Cartesian coordinates as separate equations for the x, y, and z components:

$$L_1 \sin\theta_1 \cos\phi_1 + L_2 \sin\theta_2 \cos\phi_2 + L_3 \sin\theta_3 \cos\phi_3 + L_4 \sin\theta_4 \cos\phi_4 = 0, \quad (16)$$

$$L_1 \sin\theta_1 \sin\phi_1 + L_2 \sin\theta_2 \sin\phi_2 + L_3 \sin\theta_3 \sin\phi_3 + L_4 \sin\theta_4 \sin\phi_4 = 0, \quad (17)$$

$$L_1 \cos\theta_1 + L_2 \cos\theta_2 + L_3 \cos\theta_3 + L_4 \cos\theta_4 = 0. \quad (18)$$

This set of three equations with four lengths sets the ratio of the length of each leg to the overall cavity length, assuming the chosen angles permit a closed cavity.

If the reflective phase shifts for the s and p polarizations are equal to each other at each mirror, the polarization will rotate by the same amount as the image. If the reflective phase shifts are unequal, the polarization will be altered in a more complicated way, but the polarization after one round trip can always be adjusted to match the original polarization by placing a wave plate somewhere in the cavity with properly chosen orientation and retardation.

B. Twisted-Rectangle Four-Mirror Ring

One four-mirror design with 90° image rotation is particularly promising. Figure 4 shows top, front, and side views of this design. Starting with a rectangle lying in the $(y–z)$ plane, we twist it so the corners are displaced in the directions indicated by the arrow head and tail symbols. After twisting, legs 1 and 3 tilt by α with respect to the $(y–z)$ plane whereas legs 2 and 4 tilt by β relative to this plane. Figure 5 is the corresponding unit-sphere depiction. The symmetry of this cavity implies that the four triangles making up the quadrilateral are congruent. If we demand an image-rotation angle of 90°, the area theorem outlined above implies

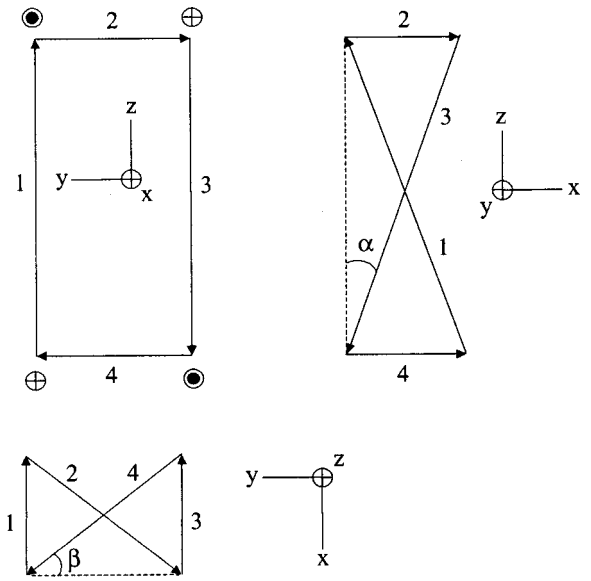

Fig. 4. Diagram of the RISTRA resonator viewed from the top, side, and end, showing how α and β are defined.

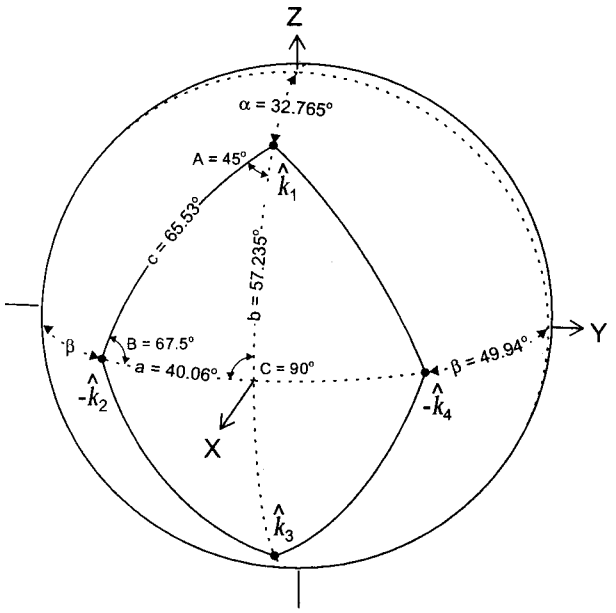

Fig. 5. Unit-sphere diagram of the RISTRA resonator. The spherical quadrilateral is symmetric to reflection in the $X–Z$ and $X–Y$ planes. All sides are equal to 65.53°, so all mirrors have 32.8° angles of incidence. The image-rotation angle is 90°.

$$4(A + B + C - \pi) = \pi/2, \quad (19)$$

$$A + B = 5\pi/8. \quad (20)$$

If we further restrict angle A to be 45°, then angle $B = 67.5°$. This choice of 45° for A makes the plane containing legs 1 and 4 perpendicular to that containing legs 1 and 2. This is attractive for an OPO because the s polarization at mirror 1 (reflecting leg 4) becomes the p polarization at mirror 2 (reflecting leg 1). Similarly, the plane containing legs 2 and 3 is perpendicular to that containing legs 3 and 4, so the s and p polarizations are also exchanged between mirrors 3 and 4. The polarizations are not reversed between mirrors 2 and 3 or between mirrors 4 and 1, however, because $B \neq 45°$.

Knowing angles A, B, and C, we can find the length of arcs a, b, and c using the cosine law for spherical triangles,

$$\cos A = -\cos B \cos C + \sin B \sin C \cos a, \quad (21)$$

and similar equations for b and c. This gives

$$a = \arccos\left(\frac{1}{\sqrt{2}\sin\frac{3}{8}\pi}\right). \quad (22)$$

Using $a = (\pi/2 - \beta)$, we find $\beta = 49.94°$. The corresponding equation for b gives $\alpha = 32.765°$, and that for c gives $c = 65.53°$. The angle of incidence on all four mirrors is $c/2$ or 32.765°.

The ratio of lengths of the short to long legs is given by

$$L_1 \sin\alpha = L_2 \sin\beta, \quad (23)$$

so $L_2/L_1 = 1/\sqrt{2}$.

An implementation of this design (in mirror image) is shown in Fig. 6. We dub this rotated-image, singly resonant, twisted-rectangle cavity a RISTRA cavity. Various configurations of crystals and beam entry and exit points are possible for RISTRA OPOs. Perhaps the simplest is with a nonlinear crystal(s) in leg L_1, with the pump beam entering through M_1 and exiting through M_2. Mirror M_2 is the signal output coupler, and the other three mirrors are high reflectors for the signal and low reflectors for the idler. The nonlinear crystal(s) is oriented so its *e* and *o* polarizations lie in the orthogonal planes of incidence for mirrors M_1 and M_2, as shown in Fig. 6. Because the *s* and *p* planes are also reversed between mirrors M_3 and M_4, if these two mirrors are identical, any reflective phase shift between *s* and *p* on reflection at M_3 is counteracted by the phase shift at mirror M_4. Thus starting at the crystal and following a horizontally polarized signal wave around the cavity, the half-wave plate in leg 2 changes the polarization to vertical. Mirrors M_3, M_4, and M_1 rotate the polarization in the same fashion as they rotate the image because of the cancellation of phase shifts between M_2 and M_3; hence the polarization is rotated back to horizontal after mirror M_1. After one trip around the cavity, the horizontally polarized wave returns as a horizontally polarized wave. The eigenpolarizations of the cavity are thus the *e* and *o* polarizations of the crystals. Without the cancellation of reflective *s* and *p* phase shifts at mirrors M_2 and M_3, a more exotic wave plate would be necessary to maintain the polarization.

If we wish to place crystals in both of the long legs, L_1 and L_3, we must use half-wave plates in both L_2 and L_4, rotated to 22.5° rather than 45°, in order to maintain linear polarizations for both crystals. In this case, the *s* to *p* phase shifts of mirrors M_3 and M_4 do not affect the polarization because the signal wave incident upon them is either *s* or *p*. If the pump beam is directed to the second crystal by reflecting off mirrors M_2 and M_3, the wave plate in leg 2 must have a half-wave of retardation at the pump as well as the signal wavelength in order to maintain proper pump and signal polarizations at both crystals.

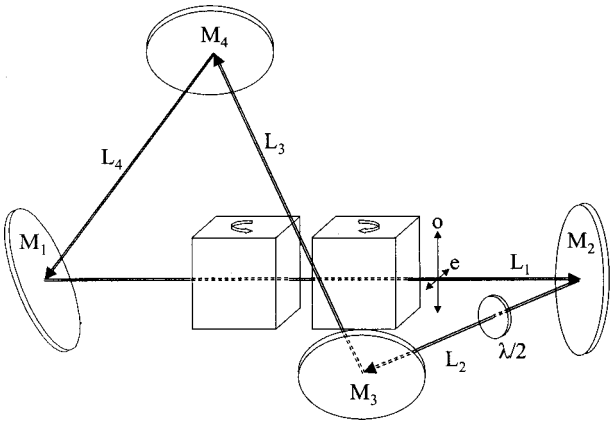

Fig. 6. Diagram of the RISTRA OPO incorporating walk-off-compensating nonlinear crystals. Legs L_1 and L_2 lie in the horizontal plane; legs L_1 and L_4 lie in the vertical plane. The eigenpolarizations of the crystal and the cavity lie in the horizontal and vertical planes.

In addition to allowing the use of a single half-wave plate for single-crystal OPOs, the RISTRA design also has the desirable feature of allowing large beams to clear the crystals while keeping the cavity relatively short because the incidence angles are large (32.765°) at each mirror.

C. General Properties of an Image-Rotating Cavity

Ring cavities, whether image-rotating or not, have several advantages over standing-wave cavities for OPO applications. With a ring there is no reflection of the pump beam back into the pump laser as there is in a standing-wave cavity with a double-passed pump. Such double pumping is required in large-Fresnel-number standing-wave OPOs if good beam quality and good beam pointing are desired.[8] In addition, because ring OPOs are unidirectional, the high irradiances at the antinodes of the standing waves are avoided, reducing the likelihood of optical damage to OPO mirrors and crystals. Unidirectional operation also reduces the amount of optical isolation required if a cw laser is used to injection seed the OPO cavity.

Further advantages specific to image-rotating rings include averaging over pump inhomogeneities. On four successive cavity passes, an off-axis ray in the signal beam samples four different parts of the pump beam. Averaged sampling of the pump beam is further enhanced if there is Poynting vector walk-off between the signal and the pump beams. These beam cleanup mechanisms enhance the principal mechanism of the development of signal/idler-field correlation zones[4] induced by nonparallel signal and idler Poynting vectors. Another advantage specific to image-rotating OPOs is their insensitivity to mirror tilts. Following the method of Anan'ev,[9] we will show that these cavities have a unique axis, and we will see how this axis is affected by a mirror tilt or by a beam displacement such as might be caused by tilting a nonlinear crystal in one leg of the cavity. We construct a vector describing the position and tilt of a ray at one location in the cavity and transform that vector to account for propagation once around the cavity, with the constraint that the final ray match the initial one both in position and tilt. The solution to this equation defines the position and the tilt of the cavity axis. We specify the beam position by x and y and the tilt by α_x and α_y. Propagation around a cavity with 90° clockwise image rotation is described by

$$\begin{bmatrix} x' \\ y' \\ \alpha_x' \\ \alpha_y' \end{bmatrix} = \begin{bmatrix} 0 & -1 & 0 & 0 \\ 1 & 0 & 0 & 0 \\ 0 & 0 & 0 & -1 \\ 0 & 0 & 1 & 0 \end{bmatrix} \begin{bmatrix} 1 & 0 & L & 0 \\ 0 & 1 & 0 & L \\ 0 & 0 & 1 & 0 \\ 0 & 0 & 0 & 1 \end{bmatrix} \begin{bmatrix} x \\ y \\ \alpha_x \\ \alpha_y \end{bmatrix}, \tag{24}$$

where L is the cavity length. Setting the initial and final vectors equal yields the equations

$$x + y + \alpha_y L = 0, \tag{25}$$

$$x - y + \alpha_x L = 0, \tag{26}$$

$$\alpha_x + \alpha_y = 0, \tag{27}$$

$$\alpha_x - \alpha_y = 0, \tag{28}$$

which has the solution

$$x = y = \alpha_x = \alpha_y = 0 \tag{29}$$

defining the cavity axis. If we consider a reference plane just after reflection from one of the mirrors and tilt that mirror by ϕ_x in the x direction and by ϕ_y in the y direction, that is, change the starting vector to

$$\begin{bmatrix} x' \\ y' \\ \alpha_x' + 2\phi_x \\ \alpha_y' + 2\phi_y \end{bmatrix}, \tag{30}$$

these equations become

$$x + y + (\alpha_y + 2\phi_y)L = 0, \tag{31}$$

$$x - y + (\alpha_x + 2\phi_x)L = 0, \tag{32}$$

$$\alpha_x + \alpha_y + 2\phi_y = 0, \tag{33}$$

$$\alpha_x + 2\phi_x - \alpha_y = 0, \tag{34}$$

with the solution

$$x = -L\phi_x, \tag{35}$$

$$y = -L\phi_y, \tag{36}$$

$$\alpha_x = -\phi_x - \phi_y, \tag{37}$$

$$\alpha_y = \phi_x - \phi_y, \tag{38}$$

defining the new cavity axis. Thus the cavity axis shifts its position by approximately L times the mirror-tilt angle, and it acquires a tilt approximately equal to the mirror tilt. A similar analysis for a beam displacement by δ_x in the x direction, such as might be introduced by tilting a nonlinear crystal within the cavity, moves the axis from $(x, y) = (0, 0)$ to $(x, y) = (\delta_x/2, \delta_x/2)$, but there is no tilt of the axis and thus no change in the propagation directions in the crystal and thus no angular tuning effect. The overlap between the pump and the signal beams will be affected by the lateral shift of the signal beam unless the pump beam is repositioned to account for the axis shift. If identical crystals are placed in the two long cavity legs, they can be oriented to partially compensate for walk-off and crystal tilt, in which case the axis shifts to $(x, y) = (\delta_x/2, \delta_x[\sqrt{2} - 1]/2) = (0.5\delta_x, 0.21\delta_x)$ if the walk-off is equal in the two crystals and if they are tilted by equal amounts.

In some cases it is possible to use walk-off-compensating crystals as shown in Fig. 6 to eliminate axis shift with crystal angle tuning. As we showed through modeling[4] and as we will discuss below in the experimental section, beam-quality improvement through image rotation requires noncollinear signal and idler Poynting vectors inside the crystal(s). For collinear phase matching the signal and idler must have opposite polarizations. If the pump is *o* polarized, two crystals can be arranged for walk-off compensation without a sign reversal of d_{eff} between them.[10] If the pump is *e* polarized, the signs will be reversed. Of course, if noncollinear phase matching is used, it is possible to adjust the Poynting vectors by tilting the pump beam to achieve signal/idler walk-off for any set of polarizations, but then walk-off compensation is not straightforward.

Finally, we note that a ray tilted by δ with respect to the axis of an image-rotating cavity will spiral away from the axis, increasing its distance from the axis by δL on each pass of the cavity.

The implication of having a unique optical axis fixed relative to the cavity is that one can build a monolithic cavity with no adjustments on the individual mirrors. The optical axis is fixed in relation to a monolithic structure. Cavity alignment then consists of positioning the structure to align the axis to the desired position and tilt, for example, to optimally overlap the pump beam. Such a cavity should be much less sensitive to vibration than a standing-wave cavity with comparable rigidity.

3. LABORATORY STUDIES OF A RISTRA OPO

In this section we describe the laboratory performance of a RISTRA OPO, comparing with the predictions of our numerical OPO model[11,12] when possible, and comparing with the performance of alternative designs. Before investing in a particular design, it is prudent to predict performance with a model. We did this for fixed crystal and

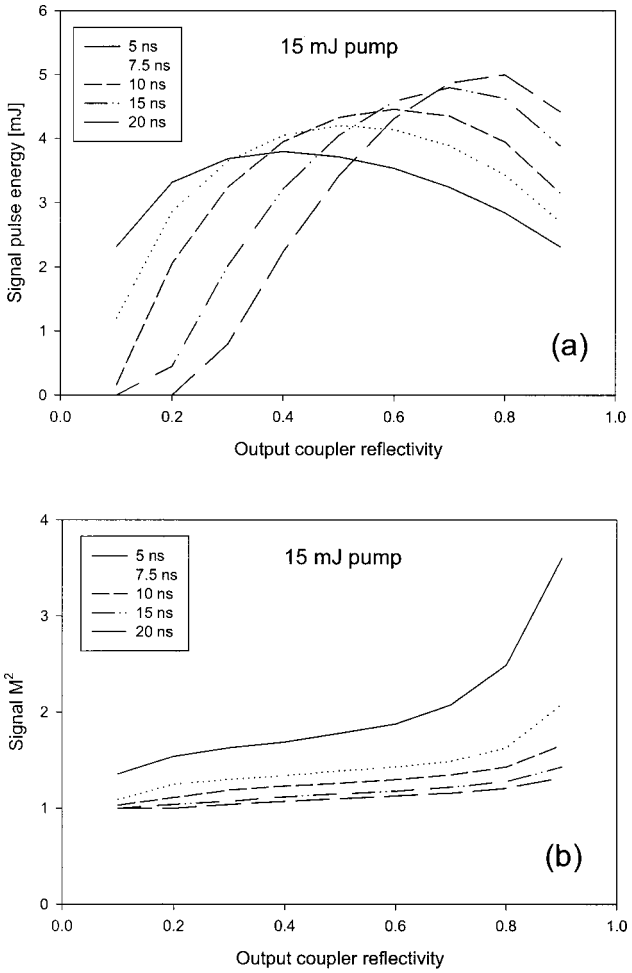

Fig. 7. Model predictions of (a) signal energy and (b) signal-beam quality factor M^2 for a 15-mJ pump pulse as a function of output-coupler reflectivity for various pump-pulse durations. The RISTRA cavity is 110 mm long with one 15-mm KTP crystal, and the pump-beam diameter is 2.1 mm $1/e^2$.

Table 1. Specifications for the Twisted-Rectangle OPO

Cavity	Design	Twisted rectangle
	Length	~107 mm
	Output coupler	$R = 0.70$ at $\lambda = 800$ nm
	Oscillation	Single-longitudinal-mode (injection seeded unless stated otherwise)
Crystal	KTP	x–z cut; $\theta = 58°$, $\phi = 0°$
	Walk-off angle	48 mrad
	Aperture	10 mm × 10 mm
	Length	15 mm
Signal	e polarization	$\lambda = 800$ nm
Idler	o polarization	$\lambda = 1588$ nm
Pump	o polarization	$\lambda = 532$ nm
Pump beam	Diameter	2–5 mm $1/e^2$
	Pulse duration	10–16 ns FWHM
	Energy	0–100 mJ
	Repetition rate	10 Hz
	Bandwidth	Injection seeded
Seed beam	Wavelength	800 nm
	Diameter	~2 mm
	Power	~1 mW
	Bandwidth	≤1 MHz

cavity lengths, namely, for a 15-mm-long KTP crystal in a 105-mm-long twisted-rectangle cavity, assuming a $1/e^2$ pump-beam diameter of 2.1 mm, and pump, signal, and idler wavelengths of 532 nm, 800 nm, and 1588 nm. We varied the pump-pulse duration and the output-coupler reflectivity to find a useful operating point. The pump-pulse energy was fixed at 15 mJ after we determined this was well above threshold throughout the useful range of the variable parameters. Figure 7 shows some predictions of our model. In the upper plot we show there is an optimum output-coupler reflectivity for each pump-pulse duration, increasing with increasing pump duration. We assumed throughout this exercise that internal cavity losses were zero. The pump-to-signal conversion efficiency tends to increase with pump-pulse duration at the optimum reflectivities, increasing from ~25% for a 5-ns pump pulse to ~35% for a 20-ns pulse. The lower plot shows the beam quality also tends to improve with the longer pump pulses, reflecting the decrease in backconversion with lower parametric gain. We chose an output-coupler reflectivity of 0.70 with the goal of maximizing efficiency as well as beam quality for a 15-ns pump pulse.

Based on these predictions, we built a RISTRA OPO with the specifications listed in Table 1 and measured its performance under two quite different conditions. First, we pumped it with a small-diameter, spatially filtered pump beam identical to that used in our earlier study of the Dove-prism OPO. We limited this study to measurements of M^2 of the signal beam for comparison with similar measurements on the Dove-prism OPO. We then switched to a large-diameter, low-quality pump beam and studied the OPO's performance in much greater detail, comparing with a three-mirror, image-inverting, ring OPO pumped by the same beam.

A. Numerical Modeling and Laboratory Measurement of M^2

Before presenting our results, we briefly discuss the matter of beam quality, or M^2. For better or worse, M^2 has become a standard for quantifying beam quality, so, following convention, we use it here. Unfortunately, M^2 is notoriously difficult to model and measure with high accuracy. Therefore to support our M^2 values, we describe our methods of predicting and measuring M^2 in detail. For numerical predictions, we begin with a small number of mesh points in the transverse grid and increase the number until adequate convergence is obtained. For small-diameter pump beams, convergence is acceptable for grids of 128×128. For large-diameter pump beams, computing constraints limit the grid size to 256×256. For this grid size, convergence for large-diameter beams is probably incomplete, implying that some of our calculated M^2 values for the large pump beam are uncertain by perhaps ± 0.2. Additionally, pulsed operation requires that one compute an M^2 that is characteristic of an entire pulse, even though the wave front evolves during the pulse. To account for this evolution, we use the adaptation of Siegman's method[13] to pulsed beams that we outlined in an earlier paper.[11]

Our measured M^2 values were determined from the second moments $\sigma_\parallel^2(z)$ and $\sigma_\perp^2(z)$ of two-dimensional signal fluence profiles recorded at various longitudinal, or z, positions spanning the waist formed by a focusing lens. Here $\parallel$ and $\perp$ denote the directions parallel and perpendicular to birefringent walk-off in the nonlinear crystal. We recorded the fluence profiles using an electronically shuttered, 10-bit, digital, progressive-scan CCD camera (Cohu 6612-3000) with a pixel spacing of 9.9 μm in both directions. By externally triggering the camera in asynchronous mode, simultaneous integration of all pixels occurred within a 250-μs acquisition window centered on the 10–15-ns signal pulse. This short integration time reduced contributions from low-level background light, and, when combined with 10-bit digitization, allowed quieter, higher-resolution measurements than those from conventional analog-camera beam-profiler systems. Nevertheless, obtaining accurate $\sigma_\parallel^2(z)$ and $\sigma_\perp^2(z)$ values requires great care because they are extremely sensitive to noise in the wings due to the r^2 weighting of the second moments. To reduce the effects of random electronic noise in the camera, we recorded ten background and ten fluence profiles at each of ~20 points spanning the focus. During analysis, the ten fluence profiles were repositioned to have a common centroid and then averaged. The background was also averaged and then subtracted from the average fluence before $\sigma_\parallel^2(z)$ and $\sigma_\perp^2(z)$ were calculated. These average values accurately represent single-shot values because injection seeding the OPO and pumping at greater than 3 times threshold, as was the

case for most of our measurements, produces stable, reproducible spatial fluence profiles with rms fluctuations in energy of only 1–2%.

Experimental errors in M^2 were estimated by varying the size of the rectangular area of CCD pixels, called an area of interest (AOI), within which each $\sigma_{\parallel}^2(z)$ and $\sigma_{\perp}^2(z)$ are calculated. For a perfect Gaussian beam and with no electronic noise, M^2 would be independent of the AOI size as long as it is large enough to encompass the entire spatial profile. In practice, $\sigma_{\parallel}^2(z)$ and $\sigma_{\perp}^2(z)$ do depend on AOI size, so, during analysis, we select various AOI sizes to calculate each $\sigma_{\parallel}^2(z)$ and $\sigma_{\perp}^2(z)$. We then choose what we judge as the most likely values of $\sigma^2(z)$ and assign an uncertainty determined by its variation with AOI size. Based on these results, $M_{\parallel}^2$ and $M_{\perp}^2$ are calculated with a nonlinear least-squares fit to the second-moment-derived waist sizes $w_{\parallel}(z) = 2[\sigma_{\parallel}^2(z)]^{1/2}$ and $w_{\perp}(z) = 2[\sigma_{\parallel}^2(z)]^{1/2}$. This procedure returns $M_{\parallel}^2$ and $M_{\perp}^2$ along with the associated waist sizes $w_{0_{\parallel}}$ and $w_{0_{\perp}}$ and waist locations $z_{0_{\parallel}}$ and $z_{0_{\perp}}$. Typical reported uncertainties in M^2 are $\pm 10\%$. We validated the entire procedure by obtaining $1.01 \leqslant (M_{\parallel}^2, M_{\perp}^2) \leqslant 1.05$ for pulsed and cw beams emerging from a 2-m-long single-mode optical fiber, with the waist formed by a high-numerical-aperture multielement lens (Melles Griot 06GLC001).

B. Performance of a RISTRA OPO Pumped by a High-Quality, Small-Diameter Pump Beam

Because pump-beam quality influences OPO performance and because our earlier study of the Dove-prism OPO[6] used a high-quality pump beam, we chose to look first at the performance of a RISTRA OPO pumped by a similar beam. These measurements used a clean spatially filtered pump beam with a $1/e^2$ diameter of ~2 mm. In our previous report on the Dove-prism design, we directly compared beam quality and conversion efficiency with and without image rotation by inserting or removing the Dove prism. Due to the relatively long 150-mm cavity length necessary to accommodate the prism, the pump conversion was relatively low, typically <35% with or without the prism, at a pump fluence 4 times oscillation threshold. Although efficiency was low, improvements in beam quality at 4 times threshold were impressive. Without image rotation, $M_{\parallel}^2 \approx 1.3$ and $M_{\perp}^2 \approx 3.4$, whereas with image rotation the signal beam was highly symmetric with $M^2 \approx 1.7$ in either direction. Comparing the signal-beam quality of the RISTRA OPO with that of the Dove-prism OPO, again with pump fluence of 4 times threshold, we find a slight improvement, to $M_{\parallel}^2 \approx 1.6$ and $M_{\perp}^2 \approx 1.6$, even though the Fresnel number increased from 33 for the Dove-prism OPO to 45 for the RISTRA OPO. Figure 8 shows an example of the far-field fluence profile for the RISTRA OPO, recorded one focal length from a focusing lens. Note that the central peak of the beam is nearly a perfect Gaussian surrounded by a ring-like structure with amplitude only 1–2% that of the central peak. In the absence of this structure, M^2 would be much closer to one. In fact, when this beam is analyzed by less rigorous techniques such as the commonly used knife-edge method, $M_{\parallel}^2$ and $M_{\perp}^2$ are approximately 1.2 (Ref. 14) rather than 1.6.

When interpreting M^2 values for a nanosecond OPO, it is important to realize that optimal performance is unlikely to produce $M^2 = 1$. This is because wave-front curvature and beam diameter can change substantially during the pulse. According to our model, the signal-beam diameter is typically smallest early in the pulse, growing rapidly as the power increases, and remaining large throughout the duration of the pulse. At the same time, wave-front curvature may increase or decrease as much as a half-wave during the pulse evolution. These dynamic changes in the far-field angular distribution probably make it impossible to achieve a perfect lowest-order Gaussian beam with $M^2 = 1$.

We conclude from our comparison with the Dove-prism OPO that the RISTRA design produces slightly better signal-beam quality for otherwise identical operating conditions. We also found it easier to align. It has fewer optical surfaces, and, for a given cavity length, can accommodate larger-diameter beams and therefore a higher Fresnel number. Beam diameters in the Dove-prism

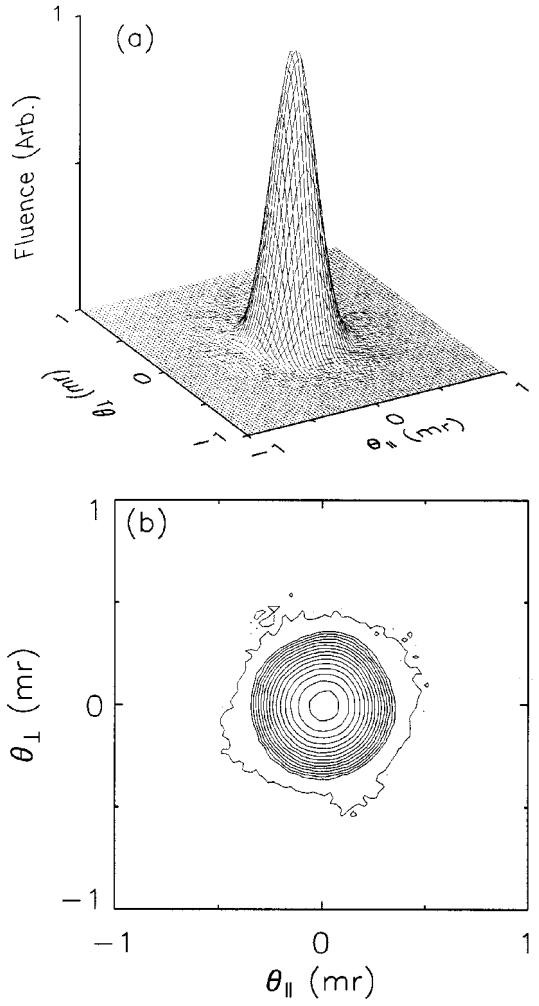

Fig. 8. Measured far-field signal fluence profile shown in (a) wire grid and (b) contour for the RISTRA OPO pumped at 4× threshold by a small-diameter (~2 mm $1/e^2$), spatially filtered pump beam. The fluence contours in the lower figure (b) are exponentially spaced to emphasize the low-level structure. The lowest contour is at 0.01 of the maximum fluence, and each contour is at 1.31 times the previous. The highest contour corresponds to 0.88 of the maximum fluence.

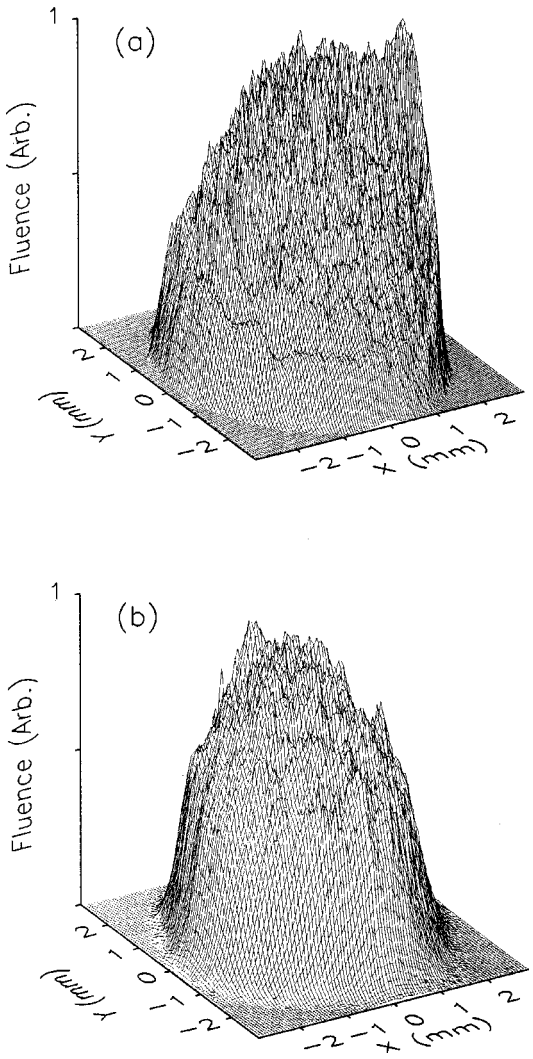

Fig. 9. (a) Large-diameter, unfiltered pump-beam fluence profile at the input to the OPO and (b) corresponding signal fluence profile at the output coupler of the OPO.

OPO are limited largely by the clear aperture of the prism. Unfortunately, an increase in that aperture also increases the length of the prism and cavity, resulting in reduced efficiency. These practical considerations limit the Dove-prism OPO to smaller-diameter beams and lower-energy pulses, whereas the RISTRA is more suited to high-Fresnel-number, high-efficiency operation.

C. Performance of a RISTRA OPO Pumped by a Low-Quality, Large-Diameter Pump Beam

High efficiency and high output energy from nanosecond OPOs requires the use of large-diameter pump beams that typically have beam quality that is less than ideal. To test the RISTRA OPO under these conditions, we imaged the exit aperture of the second of two amplifier rods in a commercial Nd:YAG laser (Continuum NY82-10) onto the input coupler of the OPO. Demagnification reduced the beam diameter from 9 mm to approximately 5 mm. The pump energy was varied with a half-wave plate and thin-film polarizer combination that does not affect the pump-beam spatial or temporal profiles. Figure 9(a) shows the pump-beam fluence profile at the OPO input mirror. Using interferometric techniques, we measured approximately one wave of phase distortion across its full diameter. The far-field profile of this beam is slightly astigmatic, as shown in Fig. 10. Measurements of M^2 along the directions of the tangential and sagittal planes returned M^2 values of, respectively, ~1.8 and ~2.0. The 5-mm diameter of this pump beam makes the Fresnel number of our cavity approximately 300.

1. Collinear Phase Matching: Parallel Idler and Pump Poynting Vectors

For the RISTRA OPO, we expect the best signal-beam quality when the pump and idler waves have parallel Poynting vectors, with the Poynting vector for the signal wave tilted with respect to them. This fulfills the requirement that the signal and idler have nonparallel Poynting vectors[4] while allowing the idler beam to carry away phase distortions that may be present in the pump beam without distorting the signal wave. This condition is achieved in our OPO for collinear phase matching of the *o*-polarized pump and idler waves with the *e*-polarized signal wave. The signal walk-off is 48 mrad or 0.72 mm

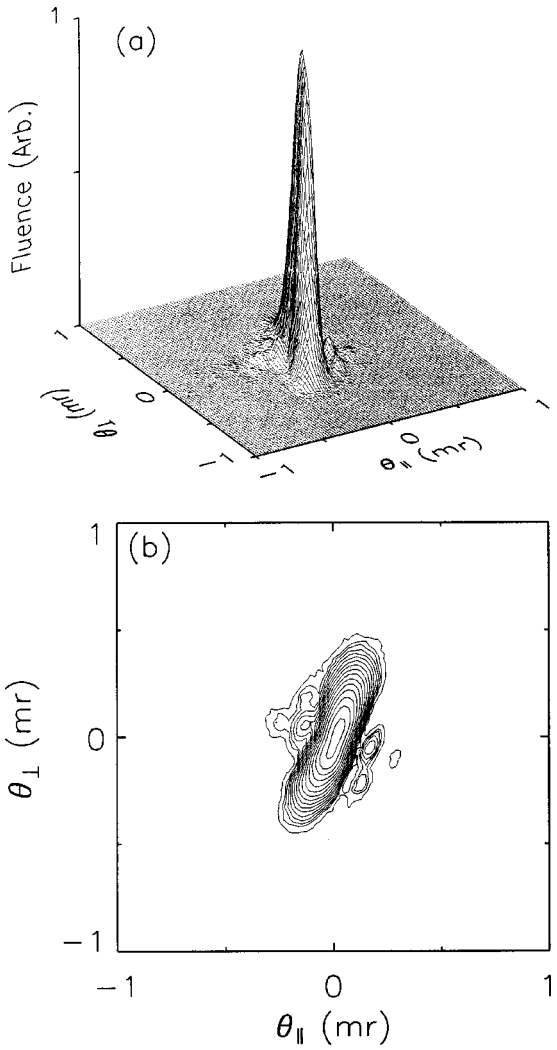

Fig. 10. Far-field pump fluence profile shown in (a) wire grid and (b) contour. The contours are exponentially spaced as in Fig. 8.

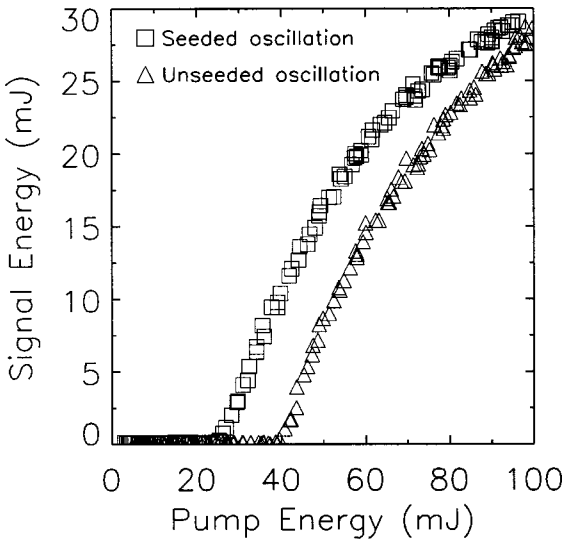

Fig. 11. Signal energy versus pump energy for the seeded and unseeded RISTRA OPO pumped by the large-diameter pump beam.

through the 15-mm-long crystal. Under these conditions, we obtain at the OPO output mirror the signal beam shown in Fig. 9(b) for operation at 4 times threshold. It is considerably more symmetric and uniform than the pump beam due to the cleanup mechanisms discussed above. Further, the efficiency is quite good, as shown in Fig. 11. For 100 mJ of 532-nm pump we generate 28 mJ of 800-nm signal for a quantum efficiency of 42%. Figure 12 shows the seeded far-field signal irradiance profile at 3 times threshold, or 70 mJ. Corresponding beam-quality measures are $M_{\parallel}^2 \approx 3.1$ and $M_{\perp}^2 \approx 3.2$ based on second-moment measurements, or $M_{\parallel}^2 \approx 2.6$ and $M_{\perp}^2 \approx 2.7$ based on knife-edge measurements.[14] Figure 13 shows typical fits to second-moment and knife-edge waists with the same set of data. It is clear that the data are of high quality and that the primary difference between the two measurements occurs near the focus where the knife-edge method understates the beam size.

When we calculate a far-field signal fluence using the measured pump fluence in our numerical OPO model, we predict a far-field angular distribution with a central lobe identical to that observed but with the structure surrounding the central lobe less structured and lower in amplitude, closely resembling an Airy pattern. This is consistent with the observation that in the near field the spatial profile of the signal beam approximates a top hat. The calculated M^2's are approximately 2 rather than the measured 3.1 and 3.2. We have not identified the source of this discrepancy, but several mechanisms that might contribute are absent in the model. For example, the model neglects phase-front distortion of the pump, assuming it has a uniform phase. For the measured pump distortion of about one wave, we expect little difference compared with a uniform phase. To experimentally check the sensitivity of the signal far-field profile to pump-beam phase distortions, we further distorted the pump phase by about one wave and found it produced barely detectable changes in the signal far-field profile. We added the pump distortion by inserting a microscope slide coated with a thin layer of UV-curing glue 50 mm before the OPO. We inspected the slide in a Mach–Zehnder interferometer to select a region that exhibited approximately one wave of distortion. This added distortion must degrade the quality of the idler beam, but we did not measure that.

Our model also neglects time variation of the pump's spatial profile. In fact, we observe considerable evolution of the pump profile at the OPO. It turns on first at the center of the beam and later at the perimeter. The delay is about equal to the pulse duration of 15 ns, so early in the pulse the pump has a diameter less than 5 mm, and late in the pulse it is a ring. This may explain our observation that the time profile of the signal far-field shoulder is double peaked with peaks early and late in the signal pulse. This seems like a plausible explanation of the excess energy in the shoulder relative to the model predictions as well at the reduced beam quality.

Finally we note that, for all the data presented in this paper, one of the RISTRA mirrors was slightly distorted. We later corrected this, and the azimuthal structure in the shoulder was substantially reduced. The total energy in the shoulder did not change much, however, nor did the values of M^2.

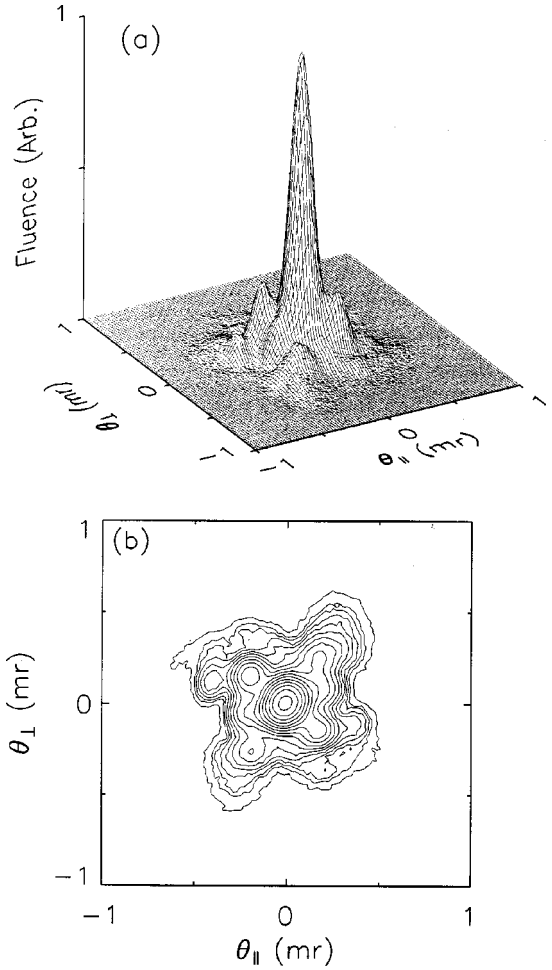

Fig. 12. OPO is injection seeded with parallel idler and pump Poynting vectors. The far-field signal fluence profile in (a) wire grid and (b) contour for the RISTRA OPO pumped at 3× threshold by the large-diameter pump. The contours are exponentially spaced as in Fig. 8.

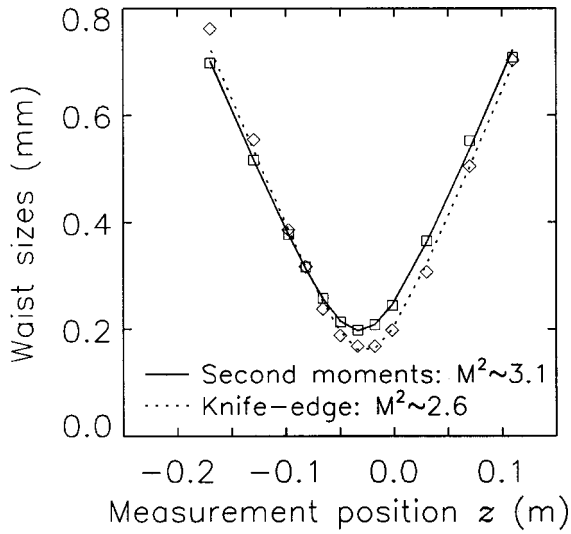

Fig. 13. Second-moment data (squares) and least-squares fit (solid curve), plus knife-edge data (diamonds) and least-squares fit (dashed curve) for the experimental conditions of Fig. 12.

It is reasonable to ask whether injection seeding the OPO is partly responsible for the high beam quality. Perhaps the seed light induces the signal beam to have a relatively flat phase across the beam. We find that blocking the seed light reduces the signal level somewhat, but it barely changes the far-field profile, as may be seen by comparing Figs. 12 and 14. Another question is whether the beam quality changes with pump level. We find that, when the pump fluence is varied from 1.5 to 4 times threshold, the signal profile changes only slightly, with a small increase in the amplitude of the shoulder. We also note that signal-beam quality changes only moderately when the pump duration is varied from 10 to 16 ns, with better beam quality associated with the longer pump pulses. For this measurement the pump-pulse duration was varied by changing the Q-switch delay of the Nd:YAG laser, rather than its flash-lamp energy, so the phase profile of the pump beam was largely unchanged. As expected, the conversion efficency improves with increasing pump duration, up to our maximum length of 16 ns. Agreement between predicted and measured signal energy with the 5-mm pump beam was better than 5%.

To emphasize the high quality of the beam obtained with the RISTRA OPO, in Fig. 15 we compare far-field signal fluence profiles from the three-mirror, image-inverting, ring OPO and the RISTRA OPO, both pumped by the large-diameter beam at 4 times threshold. The profile in Fig. 15(a) for the three-mirror ring has $M_{\parallel}^2 \approx 3.3$ and $M_{\perp}^2 \approx 8.2$ at a pump duration of 10 ns, and the profile in Fig. 15(b) from the RISTRA OPO has $M_{\parallel}^2 \approx 3.1$ and $M_{\perp}^2 \approx 3.2$ for a 16-ns pump pulse. The cavity lengths of the two oscillators were equal, but the output-coupler reflectivity was 84% for the three-mirror ring and 70% for the RISTRA OPO. Signal-pulse energies were similar for the two oscillators at 4 times threshold.

Our model also neglects the higher-order nonlinear effects of two-photon absorption and nonlinear refractive index, but the fact that the signal far-field beam profile does not change with pump energy argues against their importance, as does an estimate of their influence based on reported values of two-photon absorption[15] and nonlinear refraction coefficients.[16–18]

Finally, we note that, if the pump laser is unseeded, the beam quality of the signal wave is degraded by backconversion associated with the spikes in pump power caused by beating of longitudinal modes.

2. *Noncollinear Phase Matching: Parallel Signal and Idler Poynting Vectors*

Based on our experience in modeling image-rotating OPOs, we expect the signal-beam quality to be poorest when the signal and idler beams have parallel Poynting vectors in the crystal because there is no walk-off between the signal and idler to induce phase and amplitude correlations across the face of the beams. Our beams are large enough that diffractive coupling across the beams is also poor. We achieve parallel signal and idler Poynting vectors by tilting the pump beam in the direction of signal walk-off by

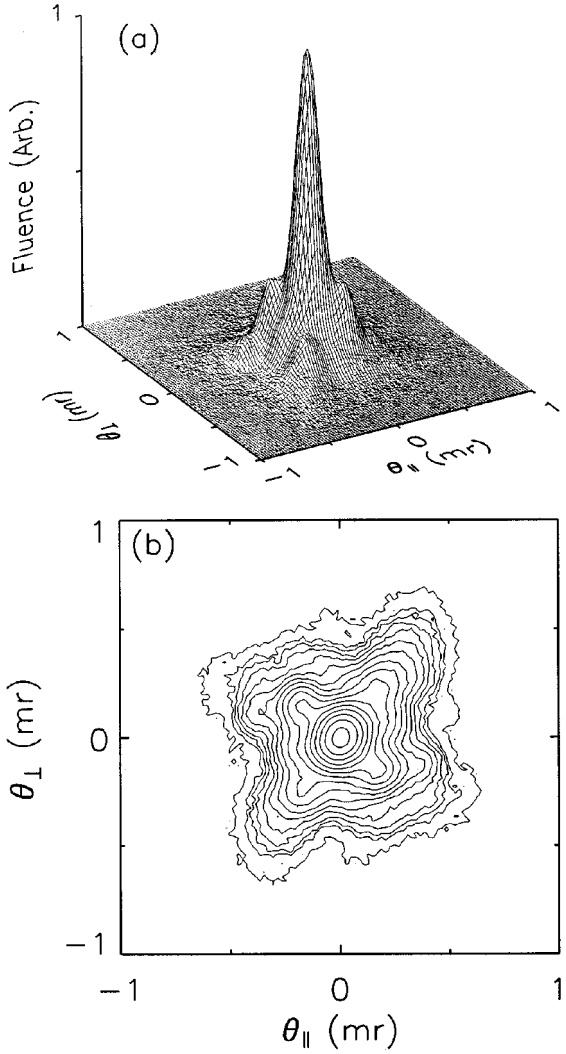

Fig. 14. OPO is unseeded with parallel idler and pump Poynting vectors. The far-field signal-fluence profile in (a) wire grid and (b) contour for the RISTRA OPO pumped at 3× the seeded threshold by the large-diameter pump. The contours are exponentially spaced as in Fig. 8.

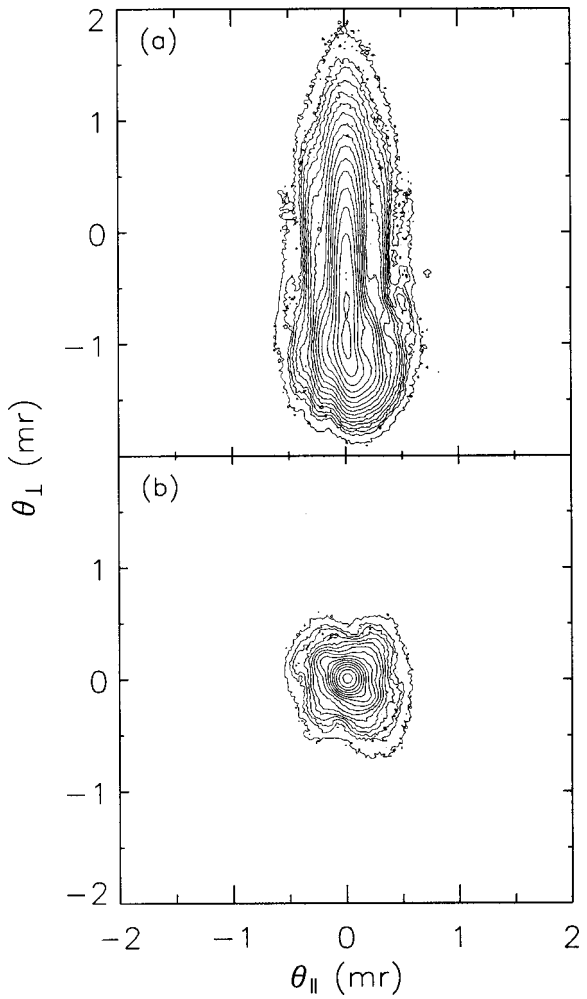

Fig. 15. Comparison of far-field signal fluence profiles for (a) three-mirror-ring image-inverting OPO and (b) the RISTRA OPO, both pumped 4× threshold with the large-diameter pump beam. Both OPOs are injection seeded, with parallel idler and pump Poynting vectors. The contours are exponentially spaced as in Fig. 8.

$$\theta_p = \rho_s \frac{\omega_i}{\omega_p} = 16 \text{ mrad}, \tag{39}$$

where ρ_s is the signal birefringent walk-off angle of 48 mrad.

Our expectation of degraded beam quality is confirmed by the measured fluence profile in Fig. 16, which is for seeded oscillation, at a pump fluence 4 times threshold. There is still a central lobe, but the energy in the shoulder is substantially higher than before. The beam profile is still reasonably good, but, comparing the fluence at the center of the far-field beam with the previous case, we find it is reduced by a factor of 3 even though the efficiencies are nearly equal. Furthermore, the beam quality is strongly influenced by the seed light in this configuration. When the seed light is blocked, the beam degrades further to the far-field distribution shown in Fig. 17.

3. Noncollinear Phase Matching: Parallel Signal and Pump Poynting Vectors

A signal with intermediate beam quality is expected when the Poynting vectors for the signal and pump waves are parallel. This provides walk-off between the signal and idler beams, but pump-phase distortions will tend to be imposed on the signal as well as the idler. This alignment is achieved by tilting the pump beam in the direction of signal walk-off by $\theta_p = \rho_s = 48$ mrad. The crystal angle is adjusted as the pump is tilted in order to maintain constant signal and idler wavelengths. If the phase and amplitude distortions of the pump beam are small, we anticipate little difference between parallel pump and signal, and the optimum case of parallel pump and idler Poynting vectors. However, in the presence of pump distortions we expect this configuration will suffer relative to the optimal case. Figure 18 shows the signal far-field fluence for this alignment for seeded oscillation at a pump level 3 times threshold. The measured M^2 values are $M_\parallel^2 \approx 3.7$ and $M_\perp^2 \approx 3.7$, indicating a beam quality comparable to collinear pumping, discussed above. When we insert the glue-coated microscope slide in the pump beam, we find that, unlike the optimal case, we see an effect on the signal far-field fluence profile. By

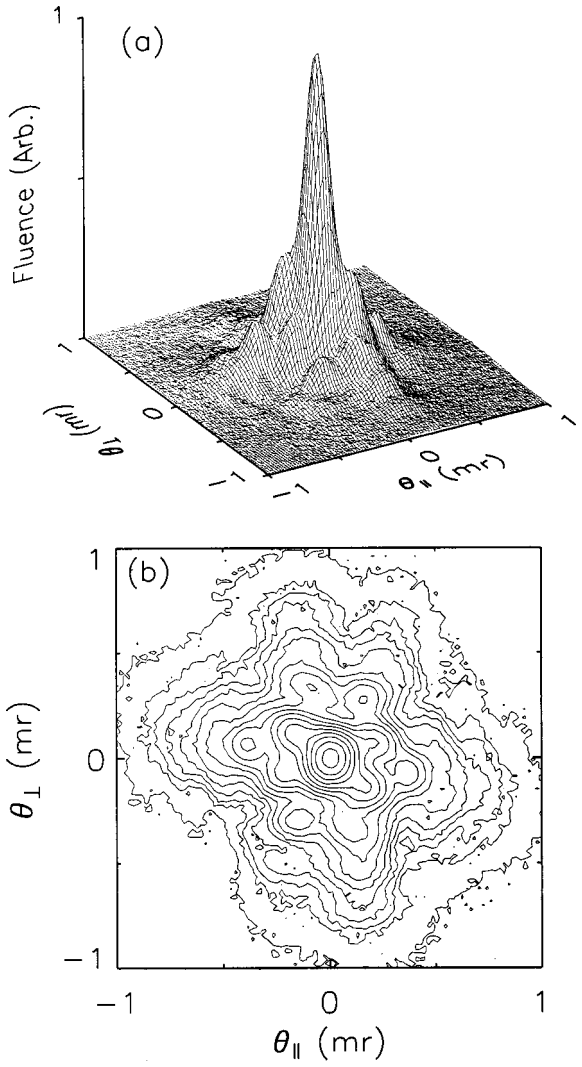

Fig. 16. OPO is injection seeded with parallel idler and signal Poynting vectors. The far-field signal fluence profile in (a) wire grid and (b) contour for the RISTRA OPO pumped 4× threshold with the large-diameter pump beam. The contours are exponentially spaced as in Fig. 8.

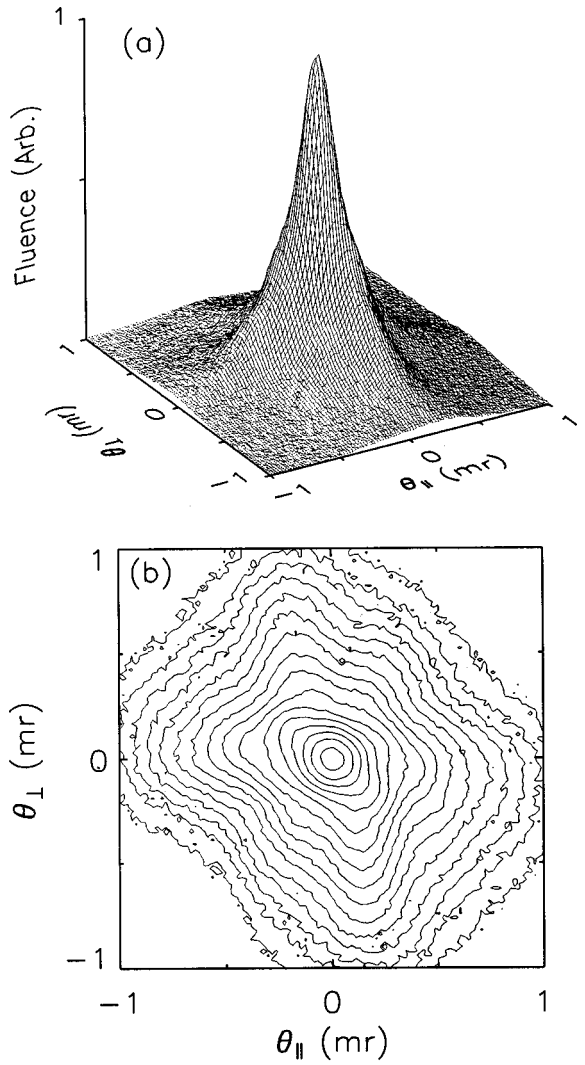

Fig. 17. OPO is unseeded and with parallel idler and signal Poynting vectors. The far-field signal fluence profile in (a) wire grid and (b) contour for the RISTRA OPO pumped 4× the seeded threshold with the large-diameter pump beam. Contours are exponentially spaced as in Fig. 8.

comparing Fig. 18, where the pump has no additional distortion, to Fig. 19, where there is added pump-phase distortion, additional structure in the shoulder in the latter figure is clearly present, including increased amplitude in a secondary ring.

Finally, we note that for all three phase-matching alignments, the signal beam always points along the cavity axis, regardless of pump tilt.

4. CONCLUSIONS

We showed how to calculate the image-rotation angle in a nonplanar ring cavity using the projection of propagation directions on the unit sphere. This knowledge was used to design a twisted-rectangle OPO with 90° image rotation, which we dub the RISTRA. The advantages of this design include those of ring cavities in general, such as greatly reduced feedback into the pump and seed lasers, and reduced likelihood of optical damage by eliminating standing waves. Additional advantages specific to image rotation include, most importantly, beam cleanup by signal/idler walk-off in the crystal, but also signal-beam cleanup by averaging over pump inhomogeneity through image rotation of the signal beam and through pump/signal walk-off in the crystal. Image-rotating cavities have the further attraction of being insensitive to mirror tilts, making possible vibration-tolerant designs such as quasi-monolithic cavities with no mirror adjustment. We demonstrated that the RISTRA OPO converts the pump efficiently, with demonstrated 42% pump depletion, while producing a high-quality signal beam. As expected, the best beam quality and efficiency are obtained when the OPO is injection seeded and the signal Poynting vector walks off from parallel pump and idler Poynting vectors. The alignment in which the idler beam walks off from parallel signal and pump beams also works well, but pump distortions are partially imprinted on the signal beam, so beam quality degrades with pump-beam quality is this configuration. The signal-beam quality is poorest when the pump walks off from parallel signal and idler

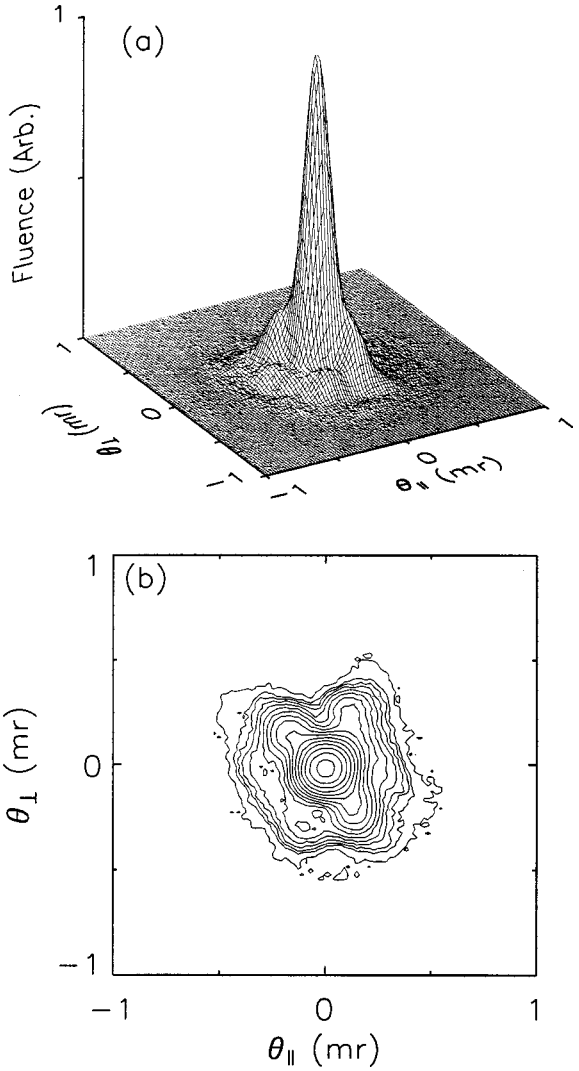

Fig. 18. OPO is injection seeded with parallel signal and pump Poynting vectors. The far-field signal fluence profile in (a) wire grid and (b) contour for the RISTRA OPO pumped 3× threshold with the large-diameter pump beam. The contours are exponentially spaced as in Fig. 8.

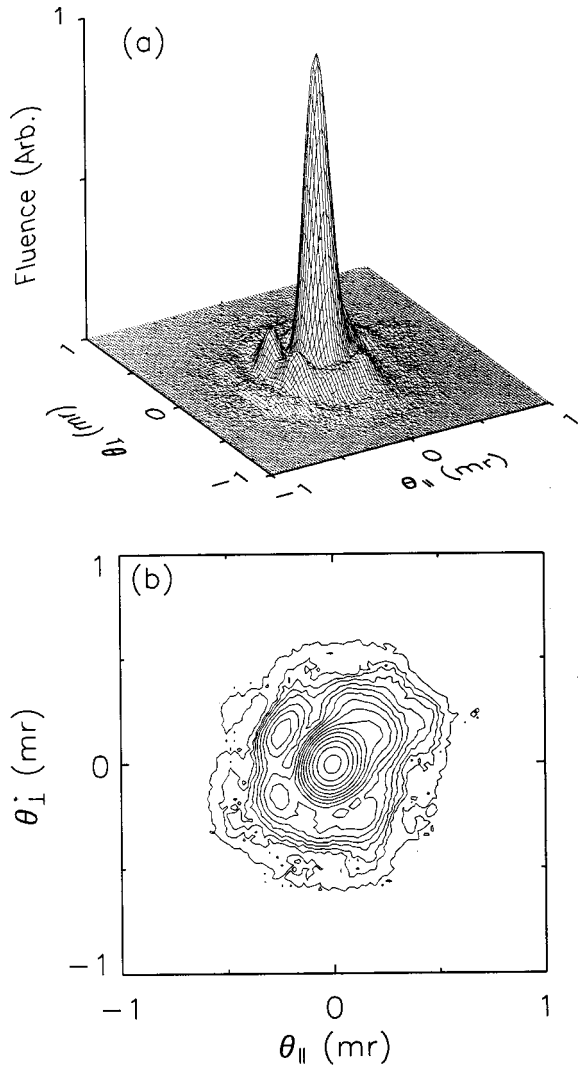

Fig. 19. OPO is injection seeded with parallel signal and pump Poynting vectors. A phase-distorting microscope slide was inserted in the pump beam 50 mm in front of the OPO input coupler. The far-field signal fluence profile in (a) wire grid and (b) contour for the RISTRA OPO pumped 3× threshold with the large-diameter pump beam. The contours are exponentially spaced as in Fig. 8.

beams. This OPO was shown to work well unseeded as well, but efficiency was reduced because of the delayed turn-on relative to the seeded OPO. The signal-beam quality tends to degrade when unseeded, but beam quality is still high relative to typical OPO designs. Pumping with an unseeded laser also tends to degrade beam quality and conversion efficiency compared with a seeded pump. The studies described in this paper were all based on a RISTRA containing a single crystal. However, the design can accommodate a second crystal in the other long leg. This can help overcome the lower parametric gain inherent with longer pump wavelengths, or it can be used to achieve earlier turn on and consequently higher conversion efficiency.

ACKNOWLEDGMENTS

This research was supported by the United States Department of Energy under contract DE-AC04-94AL85000. Sandia is a multiprogram laboratory operated by Sandia Corporation, a Lockheed Martin Company, for the United States Department of Energy.

REFERENCES

1. G. Hansson, H. Karlson, and F. Laurell, "Unstable resonator optical parametric oscillator based on quasi-phase-matched $RbTiOAsO_4$," Appl. Opt. **40**, 5446–5451 (2001).
2. J. N. Farmer, M. S. Bowers, and W. S. Scharpf, Jr., "High brightness eye safe optical parametric oscillator using confocal unstable resonators," in *Advanced Solid-State Lasers*, M. M. Feyer, H. Injeyan, and U. Keller, eds., Vol. 26 of OSA Trends in Optics and Photonics Series (Optical Society of America, Washington D.C., 1999), pp. 567–571.
3. B. C. Johnson, V. J. Newell, J. B. Clark, and E. S. McPhee, "Narrow-bandwidth low-divergence optical parametric oscillator for nonlinear frequency-conversion applications," J. Opt. Soc. Am. B **12**, 2122–2127 (1995).
4. A. V. Smith and M. S. Bowers, "Image-rotating cavity designs for improved beam quality in nanosecond optical parametric oscillators," J. Opt. Soc. Am. B **18**, 706–713 (2001).
5. G. Anstett, G. Goritz, D. Kabs, R. Urschel, R. Wallenstein, and A. Borsutzky, "Reduction of the spectral width and beam divergence of a BBO-OPO by using collinear type-II phase matching and back reflection of the pump beam," Appl. Phys. B **72**, 583–589 (2001).
6. D. J. Armstrong and A. V. Smith, "Demonstration of improved beam quality in an image-rotating optical parametric oscillator," Opt. Lett. **27**, 40–42 (2002).
7. E. J. Galvez and C. D. Holmes, "Geometric phase of optical rotators," J. Opt. Soc. Am. A **16**, 1981–1985 (1999).
8. W. J. Alford, R. J. Gehr, R. L. Schmitt, A. V. Smith, and G. Arisholm, "Beam tilt and angular dispersion in broadbandwidth, nanosecond optical parametric oscillators," J. Opt. Soc. Am. B **16**, 1525–1532 (1999).
9. Y. A. Anan'ev, *Laser Resonators and the Beam Divergence Problem* (Hilger, London, 1992).
10. D. J. Armstrong, W. J. Alford, T. D. Raymond, A. V. Smith, and M. S. Bowers, "Parametric amplification and oscillation with walk-off-compensating crystals," J. Opt. Soc. Am. B **14**, 460–474 (1997).
11. A. V. Smith, W. J. Alford, T. D. Raymond, and M. S. Bowers, "Comparison of a numerical model with measured performance of a seeded, nanosecond KTP optical parametric oscillator," J. Opt. Soc. Am. B **12**, 2253–2267 (1995).
12. A. V. Smith and M. S. Bowers, "Phase distortions in sum- and difference-frequency mixing in crystals," J. Opt. Soc. Am. B **12**, 49–57 (1995).
13. A. E. Siegman, "Defining the effective radius of curvature for a non ideal optical beam," IEEE J. Quantum Electron. **27**, 1146–1148 (1991).
14. T. F. Johnston, "Beam propagation (M^2) measurement made as easy as it gets: the four-cuts method," Appl. Opt. **37**, 4840–4850 (1998).
15. R. DeSalvo, A. A. Said, D. J. Hagan, E. W. Van Stryland, and M. Sheik-Bahae, "Infrared to ultraviolet measurements of two-photon absorption and n_2 in wide bandgap solids," **32**, 1324–1333 (1996).
16. M. Sheik-Bahae and M. Ebrahimzadeh, "Measurements of nonlinear refraction in the second-order $\chi^{(2)}$ materials $KTiOPO_4$, $KNbO_3$, β-BaB_2O_4, and LiB_3O_5," Opt. Commun. **142**, 294–298 (1997).
17. H. P. Li, C. H. Kam, Y. L. Lam, and W. Ji, "Femtosecond Z-scan measurements of nonlinear refraction in nonlinear optical crystals," Opt. Mater. **15**, 237–242 (2001).
18. M. Sheik-Bahae, D. C. Hutchings, D. J. Hagan, and E. W. Van Stryland, "Dispersion of bound electronic nonlinear refraction in solids," IEEE J. Quantum Electron. **27**, 1296–1309 (1991).